



Influence of the geometry of partially-spanning joints on mechanical properties of rock in uniaxial compression



T. Xu ^{a,b}, P.G. Ranjith ^{b,*}, P.L.P. Wasantha ^b, J. Zhao ^b, C.A. Tang ^c, W.C. Zhu ^a

^a Center for Rock Instability and Seismicity Research, Northeastern University, Shenyang 110006, China

^b Deep Earth Energy Lab, Monash University, Building 60, Melbourne, Victoria 3800, Australia

^c College of Civil Engineering, Dalian University of Technology, Dalian 116024, China

ARTICLE INFO

Article history:

Received 27 March 2013

Received in revised form 10 October 2013

Accepted 14 October 2013

Available online 24 October 2013

Keywords:

Partially-spanning joint

Joint location

Joint orientation

Joint trace length

Jointed rock

Compressive strength

ABSTRACT

As jointed rocks consist of joints embedded within intact rock blocks, their behavior depends on the behaviors of the joints and the intact rock blocks. In a jointed rock, there are two levels of heterogeneity within the jointed rocks due to the differences in properties between the rock blocks and the joints at a macro-scale, and within the intact rock blocks due to difference in the randomly-distributed flaws at a meso-scale. In this paper, numerical tests on plane stress numerical specimens with an embedded, partially-spanning joint are reported. The individual influence of three parameters relating to the geometry of partially-spanning joints: joint location, joint orientation and trace length was studied. In the simulations, the joints were modeled by elements with low moduli and strengths, whereas the heterogeneity of the rock properties of the intact rock block was taken into account by assuming that they obey the Weibull distribution. The numerical simulations not only agreed well with the experimental results, but also duplicated the complete rupture process of samples with the stress evolution and tempo-spatial distribution of damage events. The numerical results show that there is an approximately linear relationship between the location of the terminus of the partially-spanning joint with respect to the end of the sample (joint location) and the compressive strength of the partially-cut sample, whereby failure stress increases with increasing joint location value. With respect to joint orientation, the simulations show that the minimum compressive strength occurs for a joint angle of 45°, and that compressive strength increases with both increasing joint angle and decreasing joint angle from this critical value of 45°. In relation to the joint trace length, the numerical results reveal that the compressive strength of partially-cut specimens is correlated with the joint trace length using an approximately linear relationship.

© 2013 Elsevier B.V. All rights reserved.

1. Introduction

Geotechnical engineers are actively engaged in the search for solutions to complex problems involving the behavior of jointed rocks. Jointed rocks are heterogeneous and discontinuous containing joints and/or bedding planes with varying degrees of strength along these planes of weakness. The behavior of a jointed rock is governed not only by the properties of the intact rock block, but also mostly by the presence and properties of discontinuities such as joints and/or bedding planes within the jointed rock. For example, it is essential to know if and how existing joints and/or bedding planes connect with each other to form a continuous discontinuity surface for the stability of rock slopes or tunnels (Brekke and Selmer-Olsen, 1965; Chakraborty et al., 1994). In this case, the geometry of joints such as their location, orientation

and joint trace length can heavily influence the deformability and strength of jointed rocks, which is highly relevant to fields including mining engineering, underground excavation and petroleum engineering. Therefore, it is of paramount importance to know how the geometry of joints influences the deformability and strength of jointed rocks.

Extensive experimental and numerical research has been done on the mechanical behavior of rock-like materials from a single pre-existing flaw such as a joint, weakness plane or fracture in compression. For example, Lajtai (1975) experimentally examined the influence of a single plane of weakness on shear strength in direct shear loading and found that the total shear strength of rock was determined by fundamental shear strength (cohesion) and internal friction in solid bridges and by joint friction along the separated parts of the weakness plane. Petit and Barquins (1988) studied crack propagation in sandstone from a single flaw subjected to uniaxial compression. Huang et al. (1990) performed uniaxial compression tests on marble plate with an inclined central slot, observed the initiation and propagation of primary tensile cracks and secondary tensile cracks up to ultimate failure, and identified four types of ultimate failure. Ramamurthy and Arora (1994) conducted a series of uniaxial and triaxial compression tests on

* Corresponding author at: Deep Earth Energy Lab, Bld. 60, Clayton Campus, Monash University, Victoria 3800, Australia. Tel.: +61 3 99054982; fax: +61 3 99054944.

E-mail address: ranjith.pg@monash.edu (P.G. Ranjith).

URL's: <http://eng.monash.edu.au/civil/about/people/profile/ranjithp>, <http://users.monash.edu.au/~ranjithp> (P.G. Ranjith).

Paris, Jamrani and Agra sandstones with joints varying in number and inclination and proposed a strength criterion for jointed rocks. Shen et al. (1995) performed a series of uniaxial compression tests on gypsum specimens with pre-existing fractures to study the failure mechanism of fractures and rock bridges in fractured rock masses. Bobet and Einstein (1998a) also performed uniaxial and biaxial compression tests on pre-fractured gypsum specimens, investigated the crack initiation, propagation and coalescence of two parallel flaws in gypsum specimens and observed two types of cracks: wing cracks and secondary cracks. Similar observations have been reported by Wong and Chau (1998) on model sandstone and Wong et al. (2001) on model specimens. More recently, Prudencio and Van Sint Jan (2007) performed experimental tests on physical models of rock with non-persistent joints and found that the failure modes and maximum strengths of rock samples were dependent on the geometry of the joint systems, the orientation of the principal stresses, and the ratio between intermediate stress and intact material compressive strength. Chen et al. (2012) investigated the combined influence of joint inclination angle and joint continuity factor on the deformation behavior of jointed rock mass for gypsum specimens with a set of non-persistent open flaws in uniaxial compression and revealed that the deformation behavior of the jointed rock mass was correlated to the closure of pre-existing joints, the development of fractures in the rock matrix and teeth shearing of the shear plane. Wasantha et al. (2012a) developed constitutive models to describe the influence of joint geometry on the uniaxial compressive strength of rock containing partially-spanning joints using existing experimental data from uniaxial compressive strength tests. Numerical methods have also been employed in the study of the mechanical properties of quasi-brittle rock-like materials with pre-existing fractures or joints. Ingraffea and Heuze (1980) performed finite element modeling for a numerical specimen with a single inclined flaw loaded in compression and duplicated the stable and unstable propagation of primary and secondary crack growth observed in experiments. Tang and Kou (1998) carried out numerical simulations on samples of brittle materials containing multiple pre-existing flaws using the finite element method and observed the propagation and coalescence of wing cracks in either tensile or shear mode, or a combination of both modes. Bobet and Einstein (1998b) performed numerical modeling of fracture coalescence in a model rock material using a hybridized indirect boundary element method. Using the discontinuous deformation analysis method originally proposed by Shi (1988), Lin et al. (1996) further extended the use of discontinuous deformation analysis in the study of crack growth in jointed rock. Vászárhelyi and Bobet (2000) studied crack initiation, propagation and coalescence in uniaxial compression using the displacement discontinuity method. Zhang and Sanderson (2001) evaluated the effects of fracture geometry and loading direction on the instability of fractured rock masses using a distinct element method, while Giacomini et al. (2008) investigated the flow anisotropy within a natural joint subjected to mechanical shear. Deb and Das (2009) provided a numerical example of the application of the extended finite element method (XFEM) in jointed rock samples with varying joint inclination angles. More recently, Zhang and Wong (2012, 2013) studied the cracking and coalescence behavior in a rectangular rock-like specimen containing two parallel pre-existing open flaws under uniaxial compression load using a parallel bonded-particle model. Ma et al. (2009) and Zhang et al. (2010) modeled complex crack propagation using the numerical manifold method. Wu and Wong (2012, 2013) studied the effects of the friction and cohesion on the crack growth from a closed flaw under compression using numerical manifold method.

Although considerable attention has been paid to the initiation and propagation of pre-existing flaws in jointed rock mass, the influence of joints on the overall mechanical properties of jointed rock mass and the underlying fracturing mechanism remain less well understood. Moreover, detailed knowledge of the effect of joints on the overall mechanical properties of jointed rock mass is fundamental to an

understanding of the deformation and failure process of engineering rock mass and the design of engineering rock mass structures. Thus, in the present study, an attempt has been made to consider the most significant aspects including joint location, joint orientation and joint trace length of rock joints which are mainly responsible for the reduction in strength and are measurable in the field.

2. Brief outline of numerical model

Numerical simulation is currently the most popular method used for modeling the deformation behavior of rock-like materials before failure. Even though progress has been made in the numerical simulation of failure in rocks, a satisfactory model which can simulate progressive failure in a more visual way, including simulation of the failure process and failure-induced stress redistribution, is lacking.

The demand for new tools which may contribute to a better understanding of the failure mechanisms of heterogeneous brittle materials initiated the development of the Rock Failure Process Analysis code (abbreviated as RFPA^{2D}). RFPA^{2D} is a progressive elastic damage model. It can simulate the non-linear deformation of a quasi-brittle or brittle behavior with an ideal brittle constitutive law for heterogeneous materials by incorporating the heterogeneity of material properties into the model. It can also simulate strain-weakening and discontinuum mechanics problems in the continuum mechanics mode by introducing the reduction of material parameters after element failure.

There are two levels of heterogeneity in a jointed rock, one being the differences in properties between the rock block and the joint at a macro-scale, and the other being the heterogeneity within the intact rock blocks due to differences in the randomly distributed flaws at a meso-scale. In the model, because the system was analyzed at a meso-scale, the heterogeneity within the intact rock blocks due to the differences in the degree of weathering and the randomly distributed flaws at a meso-scale was taken into account. The stress-strain relationship can be described by an elastic damage constitutive law. Continuum damage mechanics can describe the effects of progressive micro-cracking, void nucleation, and micro-crack growth at high stress levels using a constitutive law, by making use of a set of state variables modifying the material behavior at the macroscopic level. Using an isotropic continuum damage formulation, the constitutive law for an isotropic and elastic material at instantaneous loading can be written as (Lemaitre and Desmorat, 2005):

$$\varepsilon_{ij} = \frac{1+\nu}{E} \sigma_{ij} - \frac{\nu}{E} \sigma_{kk} \delta_{ij} \quad (1)$$

$$E = E_0(1-D) \quad (2)$$

where ε_{ij} is the damaged elastic strain tensor, σ_{ij} is the stress tensor, E and E_0 are the Young's modulus of the damaged and undamaged materials, respectively, D is the isotropic damage variable, ν is the Poisson's ratio and δ_{ij} is the Kronecker symbol. In the case of a uniaxial state of stress ($\sigma_{11} \neq 0, \sigma_{22} = \sigma_{33} = 0$), the constitutive relation can be rewritten in terms of the longitudinal stress and strain components only (Lemaitre and Desmorat, 2005):

$$\sigma_{11} = E_0(1-D)\varepsilon_{11}. \quad (3)$$

Hence, for uniaxial loading, the constitutive law is explicitly dependent on the damage index D .

The model is based on progressive isotropic elastic damage. Fig. 1 shows the constitutive law for an element in uniaxial compression and uniaxial tension. When the stress on an element exceeds a damage threshold, its Young's modulus E is modified according to Eq. (2). In the beginning, each element is considered to be elastic, as defined by a specific Young's modulus and Poisson's ratio. The stress-strain curve of the element is considered linear elastic with a constant residual strength until the given damage threshold is reached. The maximum tensile strain

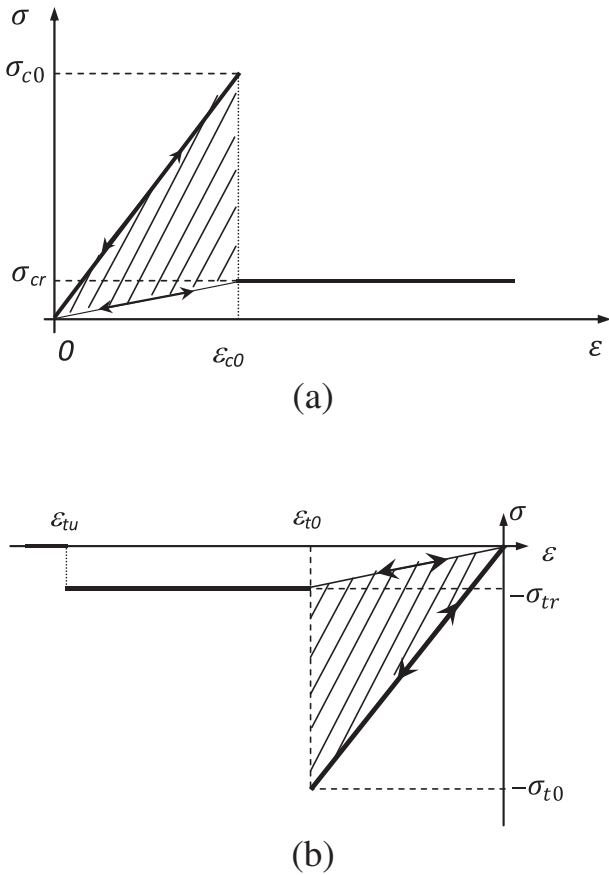


Fig. 1. Constitutive law for element in uniaxial compression (a) and uniaxial tension (b).

Brady and Brown, 2004; Jeager et al., 2007) have been selected as two damage thresholds. At any time, the tensile strain criterion is preferred since the tensile strength of rock is far lower than its compressive strength (Jeager et al., 2007).

Specifically, when the mesoscopic element is under uniaxial tensile stress, at the beginning, the stress–strain curve is linear elastic and no permanent damage occurs. When the maximum tensile strain criterion is met for a given element, the element is damaged. According to the constitutive law of mesoscopic elements under uniaxial tension, the damage evolution of element D can be expressed as (Tang et al., 2005):

$$D = \begin{cases} 0 & \epsilon < \epsilon_{t0} \\ 1 - \frac{\sigma_{tr}}{\epsilon E_0} & \epsilon_{t0} \leq \epsilon < \epsilon_{tu} \\ 1 & \epsilon \geq \epsilon_{tu} \end{cases} \quad (4)$$

where σ_{tr} is the residual uniaxial tensile strength and $\sigma_{tr} = \lambda \sigma_{t0}$ where λ is the residual strength coefficient and σ_{t0} is the uniaxial tensile strength at the elastic strain limit ϵ_{t0} . ϵ_{tu} is the ultimate tensile strain of the element. Eq. (4) indicates that an element would be completely damaged when the tensile strain of the element attains this ultimate tensile strain.

Similarly, when the element is under uniaxial compression and damaged in shear mode according to the Mohr–Coulomb criterion, the damage variable D can be described as follows (Tang et al., 2005):

$$D = \begin{cases} 0 & \epsilon \leq \epsilon_{c0} \\ 1 - \frac{\sigma_{cr}}{\epsilon E_0} & \epsilon > \epsilon_{c0} \end{cases} \quad (5)$$

where σ_{cr} is the residual uniaxial compressive strength and is defined as $\sigma_{cr} = \lambda \sigma_{c0}$. In the model, it is assumed that $\sigma_{cr}/\sigma_{c0} = \sigma_{tr}/\sigma_{t0} = \lambda$ holds

true when the mesoscopic element is under uniaxial compression or tension.

From the above derivation of the damage variable D (which is generally called the damage evolution law in damage mechanics) and Eq. (3), the damaged Young's modulus of an element at different stress or strain levels can be calculated. The unloaded element keeps its original Young's modulus and strength prior to its strength threshold. That is to say, the element can always return to its original point when unloading. It must be emphasized that when damage variable D is equal to 1, Eq. (3) stipulates that the damaged Young's modulus will be zero, which would make the system of equations ill-posed. Therefore, a relatively small value ($1.0e-05$) is given for the Young's modulus under this condition.

In addition, in the model a single damage event represents a micro-crack-forming event to assess the damage evolution, and the damage energy release is related to the strain energy of the element before and after its damage. Therefore, the number of damage events is counted by the number of damaged elements and the damage energy release can be determined from the area of shadow shown in Fig. 1. The damage energy release from an individual damaged element in uniaxial compression can be expressed as follows:

$$e_f = \frac{(\lambda-1)\sigma_{c0}^2}{2\lambda E} V_e \quad (6)$$

and the cumulative damage energy can be obtained from the strain energy release of damaged elements:

$$\sum e_f = \frac{(\lambda-1)V_e}{2\lambda} \sum \frac{\sigma_{c0}^2}{E} \quad (7)$$

where E is the elastic modulus of the individual element, V_e is the volume of the individual element, and σ_{c0} is the uniaxial failure strength of the individual element. Similarly, the damage energy release from an individual damaged element $\frac{(\lambda-1)\sigma_{t0}^2}{2\lambda E} V_e$ and the cumulative damage energy $\frac{(\lambda-1)V_e}{2\lambda} \sum \frac{\sigma_{t0}^2}{E}$ in uniaxial tension can also be obtained. After each damage event, we update the damage, the stress, and the strength of each element. Thus, by recording the counts of failed elements, the damage evolution associated with the progressive failure can be simulated in the model.

In relation to material heterogeneity, material properties such as failure strength σ , and elastic modulus E_c for elements are randomly

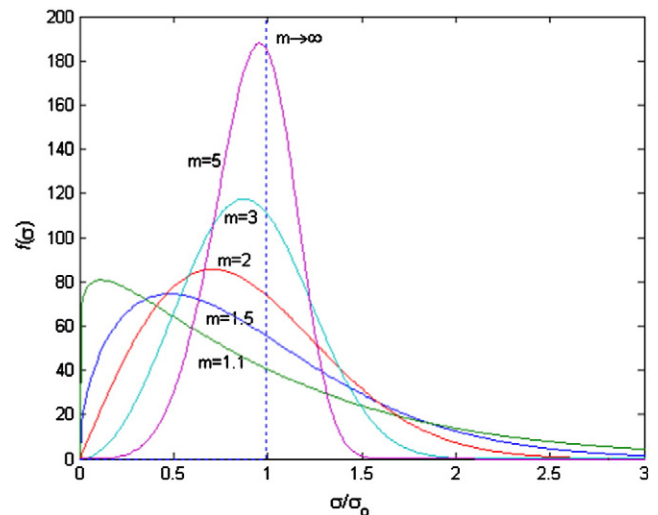


Fig. 2. Weibull distribution for element failure strength.

distributed throughout the specimen following a statistical Weibull distribution (Weibull, 1951) as shown in Fig. 2.

$$f(u) = \frac{m}{u_0} \left(\frac{u}{u_0}\right)^{m-1} \exp\left[-\left(\frac{u}{u_0}\right)^m\right] \quad (8)$$

where u is the mechanical parameter of individual element such as failure strength or elastic modulus and u_0 is a scale parameter relative to the mechanical parameter of all elements, i.e., the mean mechanical property of the elements for the specimen m is defined as the homogeneity index of the material. According to the definition, a larger m implies a more homogeneous material and vice versa. More details about the application and description of the numerical model can be found in Tang et al. (2008), Tang et al. (2006), and Xu et al. (2012).

3. Numerical model set-up

In this study, a numerical scheme identical to the experimental tests conducted by Wasantha et al. (2012b) was designed to investigate the influence of the location, orientation and trace length of partially-spanning joints on the mechanical behavior of rock-like materials loaded under uniaxial compression. A plane stress numerical specimen 168 mm in length and 84 mm in width was set up and discretized into 336×168 (56,448) elements, in which all the elements are square-shaped meshes having the same size in scale. The elements are characterized by their mechanical properties such as uniaxial compressive strength, Young's modulus, and Poisson's ratio following the statistical Weibull distribution (Weibull, 1951) at a meso-scale. The elements provide resistance against compressive or tensile deformations that are governed by the constitutive equations described above. The numerical sample contained one partially-spanning inclined joint shown in Fig. 3 and the joint location (L), joint orientation and joint trace length were changed in the simulations to investigate the effects of these factors on the mechanical behavior of rock in uniaxial compression. The width of the embedded partially-spanning joint was about 1 mm. The input material mechanical parameters for the rock block and the predefined partially-spanning

Table 1
Mechanical parameters of numerical specimen for cement mortar.

Parameter	Rock block	Joint
Homogeneity index	3	2
Mean elastic modulus (GPa)	35	5
Mean axial strength (MPa)	130	30
Poisson's ratio	0.25	0.2
Angle of internal friction (°)	38	30
Ratio of tensile to compressive strength	0.1	0.01

joint in the simulations are listed in Table 1. It is noted that the input material mechanical parameters in Table 1 at a meso-scale, which are heavily dependent on the value of the homogeneity index m , are different from the macroscopic mechanical parameters in laboratory tests and were determined by trial and error from the laboratory results. Specifically, the initial assessment values for mean elastic modulus and mean axial strength were determined according to the given macroscopic elastic modulus and axial strength of samples from an empirical formulation as shown below (Tang et al., 2003b):

$$\frac{\sigma_c}{\sigma_{c0}} = 0.2602lnm + 0.0233 \quad (1.2 \leq m \leq 50) \quad (9)$$

$$\frac{E}{E_0} = 0.1412lnm + 0.6476 \quad (1.2 \leq m \leq 50) \quad (10)$$

where E_0 and σ_{c0} are the mean elastic modulus and mean axial strength at a meso-scale, E and σ_c are the macroscopic elastic modulus and macroscopic axial strength obtained from laboratory tests, and m is the heterogeneity index. We can obtain numerically simulated elastic modulus and axial strength from a given sample with initial assessment values of mean elastic modulus and mean axial strength and adjust the input mean elastic modulus and mean axial strength for numerical samples against the known elastic modulus and axial strength from laboratory tests. In this way the macroscopic elastic modulus and macroscopic axial strength obtained from laboratory tests can be approximated from the input mean elastic modulus and mean axial strength at a meso-scale for numerical samples. In the simulations, the lower end of the numerical sample was constrained in the vertical displacement direction and an external displacement at a constant rate of 0.002 mm/step in the axial direction was applied to the upper end of the numerical sample. The stress acting on the numerical sample as well as the induced deformation in each element was computed, and the number of damage events and the associated energy release were recorded in each running step of the numerical tests.

In order to eliminate the effect of elements' spatial distribution on the numerical results, the material distributions in numerically generated matrix specimens for different cases are the same. The given partially-spanning joint was then configured in the matrix specimen. That is to say, the matrix specimens were identical, except for the variation of the partially-spanning joint. This is impossible to achieve in laboratory tests but can be achieved in a numerical test, and this is one of the advantages of numerical simulations. The detailed geometrical configurations for the different locations, orientations and trace lengths of the partially-spanning joint in the matrix specimen are presented in Fig. 4. For clarity, the samples with various joint locations are consecutively named JL1, JL2, JL3, JL4 and JL5 for joint locations of 25 mm, 35 mm, 45 mm, 55 mm and 70 mm. Similarly, the samples with various joint orientations are consecutively named JO1, JO2, JO3, JO4 and JO5 for joint orientations of 75°, 60°, 45°, 30° and 15°, and the samples with various joint trace length are named JTL1, JTL2, JTL3, JTL4 and JTL5 for joint trace lengths of 33.6 mm, 50.4 mm, 67.2 mm, 84 mm and 126 mm.

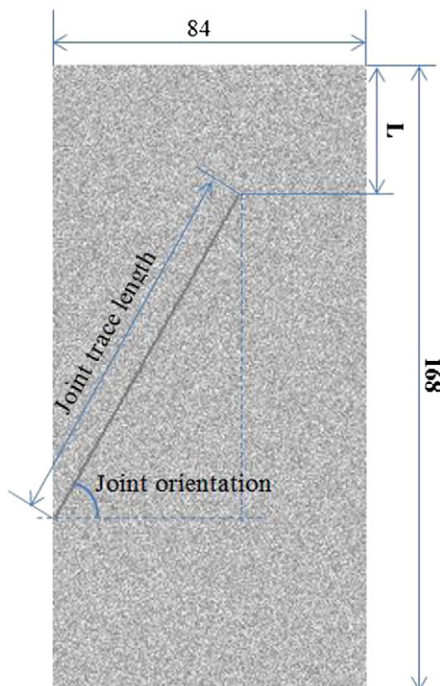


Fig. 3. Numerical sample with a partially-spanning joint.

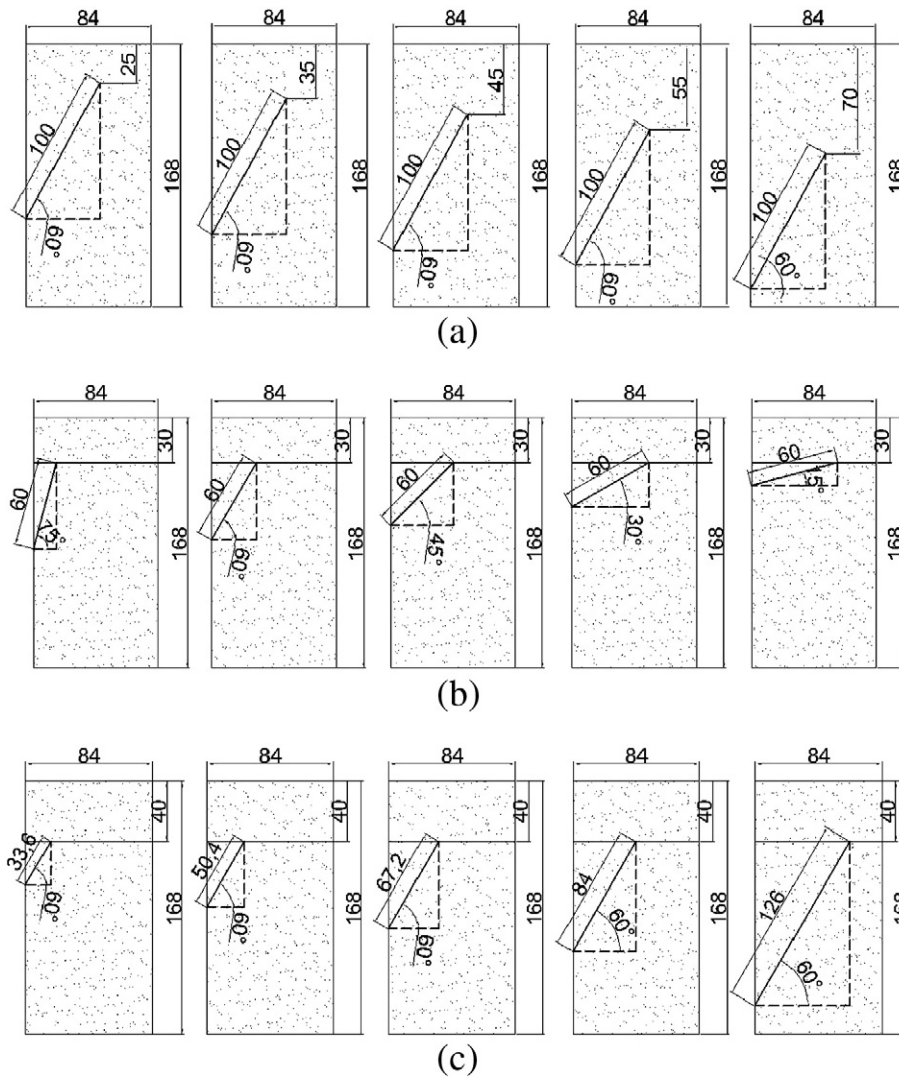


Fig. 4. Partially-spanning joint geometries with different joint locations (a), orientations (b) and trace lengths (c).

4. Modeling results and discussion

As discussed above, the uniaxial compressive testing scheme was designed to investigate the independent influence of three variables relating to the geometry of partially-spanning joints, i.e., joint location, joint orientation and joint trace length, on the overall mechanical behavior of the numerical partially-cut samples. The numerical results relevant to these three variables and their influence on stress–strain curves, damage event evolution, failure patterns and compressive strength of the partially-cut samples are presented and discussed below.

4.1. Partially-spanning joint location

The experimental and numerical final failure stresses for the partially-cut samples with various joint locations are listed in Table 2 and the comparisons between the experimental and numerical results on the final compressive strength are shown in Fig. 5. It can be clearly seen from Fig. 5 that joint location plays a paramount role in the overall mechanical behavior such as failure stress and the final failure patterns of the partially-cut samples. It is also noted from Fig. 5 that the numerical results are consistent with the experimental results and the errors fall in a reasonable zone of less than 7%, with the exception of sample JL3 with a joint location of 35 mm. According to regression analysis (Wasantha et al., 2012b), there is a positive linear correlation, $\sigma = 0.0879L + 6.8578$, between joint location and failure stress. Fig. 5

indicates that sample JL3 with a joint location of 35 mm is likely different from the other four samples due to some error in the sample preparation in the laboratory, causing the ultimate failure stress to deviate from the predicted value.

In addition, the final failure patterns and the localized strain distributions of the partially-cut samples for experimental and numerical results are presented in Table 3. The experimental results for localized strain distribution were obtained by an optical deformation and strain measuring system (ARAMIS) which is a technique used to measure the deformation and strain of the surface of an object before and after loading, and the numerical results for strain distribution highlight the high strain localization areas during testing. The experimental and corresponding numerical results illustrate the geometry of the fractures generated to accommodate failure. It is clearly shown that the numerical results are in good agreement with the experimental findings. From the

Table 2
Comparisons between experimental and numerical results for failure stress of specimen.

Joint location (mm)	Experimental (MPa)	Numerical (MPa)	Relative error (%)
25	9.6	10.1	−5.2
35	9	10.27	−14.1
45	11	10.97	0.3
55	12.1	11.3	6.6
70	12.9	12.6	2.3

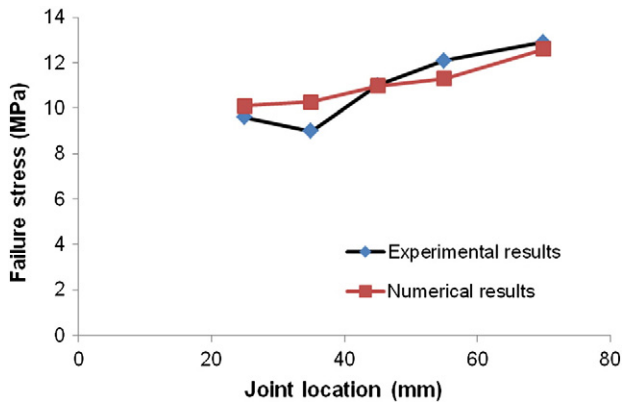


Fig. 5. Comparisons between experimental and numerical results on failure stress against joint location.

experimental and numerical failure patterns and strain distributions shown in Table 3, it can be concluded that localized deformation first took place and developed along the partially-spanning joint, and then wing cracking initiated at an acute angle with the direction of the uniaxial stress (the maximum principal stress) and grew in a curvilinear

path aligned with the compressive stress direction. The wing crack grew and coalesced to the free surface of the upper end, while secondary branch cracks along the partially-spanning joint in the specimens may form in compression. With the increase in joint location value, i.e. the distance between the terminus of the joint and the top surface of the specimen, the growth of wing cracking needs to pass a larger length of the failure path to overcome much more energy since there is larger crack continuity (Vásárhelyi and Bobet, 2000; Xu et al., 2004) or a rock bridge (Kemeny, 2003, 2005) between the terminus of the joint and the top surface of the specimen. Thus, many more secondary branch cracks may form and a higher failure stress to break the sample is reached with the increase of joint location value, as clearly illustrated in Table 3. That is to say, a larger joint location value will require a more significant amount of energy to cause propagation of the partially-spanning joint to the sample edge, allowing failure. Increasing compressive strength with increasing joint location values can therefore be explained by the larger energy input required to fail the specimen with increasing partially-spanning joint position. This is in accordance with Griffith's theory (Griffith, 1921), which indicates that the amount of energy applied to cause fracture is at least in part governed by the length of intact material that must be ruptured in the process of failure.

Fig. 6 shows the numerically simulated stress–strain curves and associated damage event counts of samples with various joint locations.

Table 3
Failure patterns for experimental and numerical results for specimens with various joint locations.

JL	25 mm	35 mm	45 mm	55 mm	70 mm
Experimental failure pattern					
Numerical failure pattern					
Experimental strain distribution					
Numerical strain distribution					

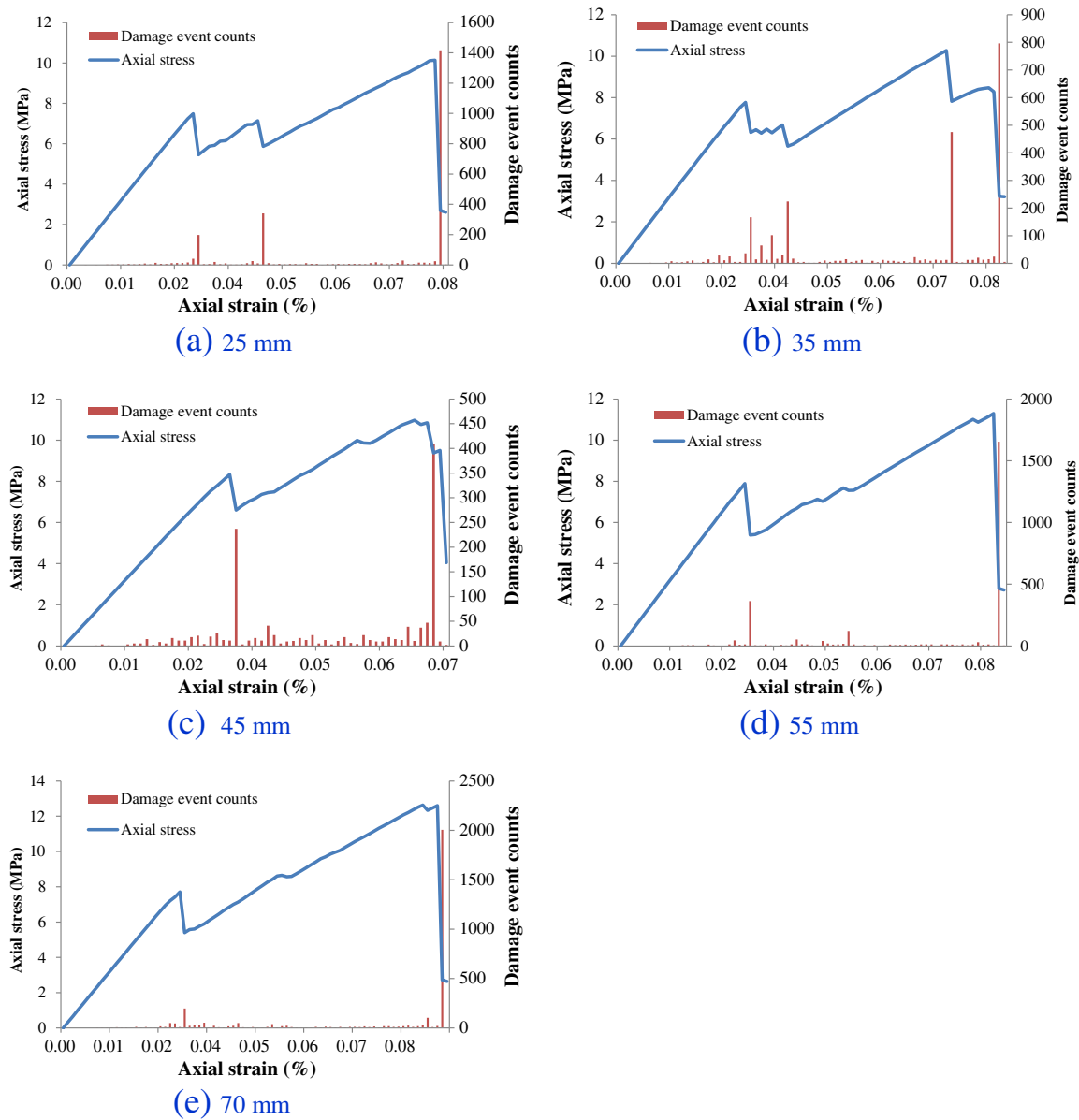
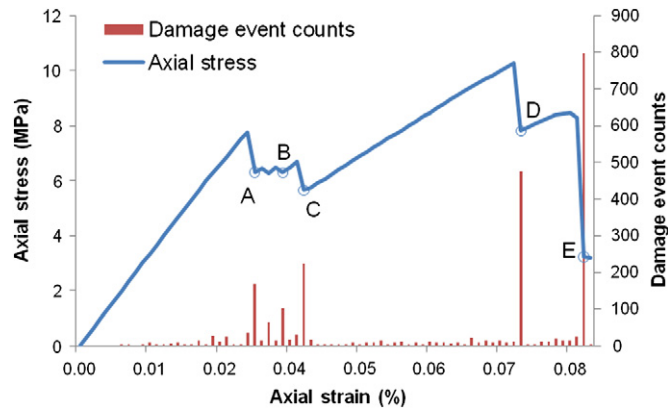


Fig. 6. Numerical stress and associated damage event counts vs. strain curves of samples with various joint locations.

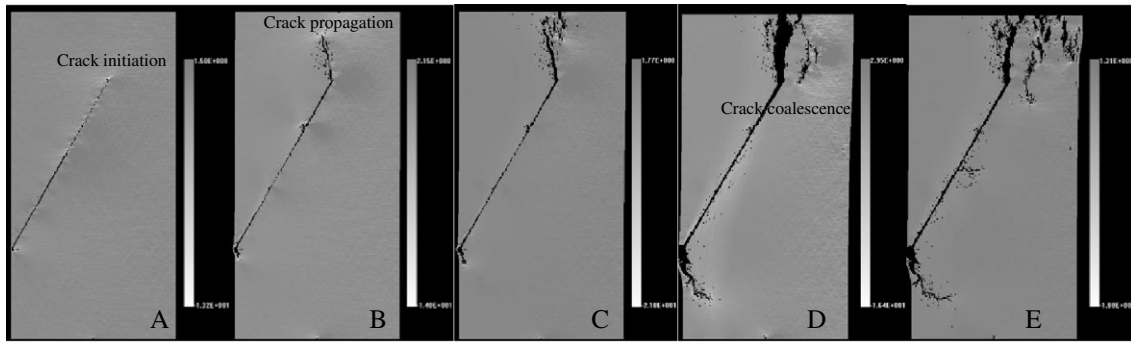
It can also be seen from Fig. 6 that joint location plays a significant role in the complete stress–strain curves of the samples. Firstly, joint location value has a significant effect on the final stress of the samples, as clearly illustrated in Fig. 5. Secondly, joint location value has little effect on the initial stiffness or Young's modulus of the samples. The initial Young's modulus results of the samples are almost the same at 28.2 GPa. Thirdly, the complete stress–strain curves of the samples have some local peaks, and each local peak or stress drop corresponds to a sudden jump in damage event counts. The more obvious the local peak or stress drop is, the greater the damage event counts correspondingly increase, and vice versa. Moreover, the lower the joint location value, the earlier a major damage event occurs at the stress–strain curve.

The complete stress–strain curve, the damage event counts–strain curve, and the corresponding stress and damage evolution at stress drops A, B, C, D and E for numerical sample JL2 are represented in Fig. 7 to illustrate the initiation, propagation, and coalescence of cracks in partially-cut samples during loading. It is seen from Fig. 7 that the weak elements first fail along the partially-spanning joint under high local stress concentration induced by compressive loading at the early stage of loading. A red circle stands for a damage event induced by

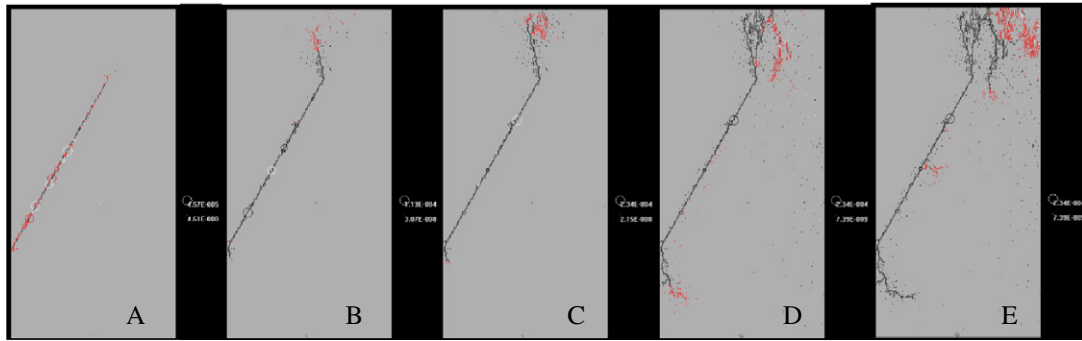
tensile stress and a white circle for a shear-induced damage event in the model. The size of the circle reveals the amount of energy release due to the damage to an element. Thus, it is clearly seen that there is tensile-induced failure as well as compressive-induced shear failure of the elements prior to stress drop A. As the compressive load continues, the high tensile stress concentrates at the tip of the partially-spanning joint and a new crack initiates and propagates in the direction of the maximum principal stress (Steif, 1984; Kemeny, 1991). The crack may either snap to a free surface or be arrested by a high-strength element, whereupon stresses are redistributed and another new crack or crush may start. This is accompanied by stress drops B and C in the quasi-static load–displacement response with dominant tensile damage events. After reaching a valley at stress drop C, a new ascending path can be found up to a new local peak, which is also the global peak for structural failure of the sample. This indicates that the applied load is mainly borne by the cut-apart sample, as we can see tensile damage events cluster at the upper part of the residual sample. Later, the sample continues to fail to a residual strength after a further loading at stress drop E. The jumpy response is difficult to trace in laboratory tests without a stiffness or servo-controlled testing machine (Hudson et al.,



(a)



(b)



(c)

Fig. 7. The stress–strain and damage event counts–strain curves (a), the corresponding tensile stress (b) and damage event evolution (c) at stress drops A, B, C, D and E for numerical sample JL2.

1971, 1972), although some indirect control schemes provide possibilities (Okubo and Nishimatsu, 1985; Fairhurst and Hudson, 1999). Numerical simulations display these local peaks associated with the sequential development of primary and secondary cracks, as also demonstrated in experimental results (Xu et al., 2003) and numerical results show that the failure of jointed samples in axial compression is

Table 4
Comparisons between experimental and numerical results for failure stress of specimen.

Joint orientation (°)	Experimental (MPa)	Numerical (MPa)	Relative error (%)
75	25.6	19.9	16.9
60	22.5	15.1	31.4
45	21.4	12.8	40.2
30	28	19.2	32.9
15	35	29.1	19.5

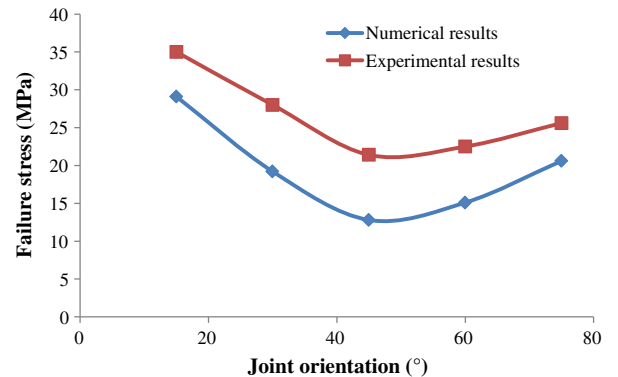


Fig. 8. Comparisons between experimental and numerical results of failure stress against joint orientation.

the final manifestation of earlier tensile crack growth induced under overall compression.






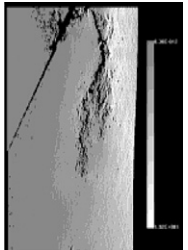
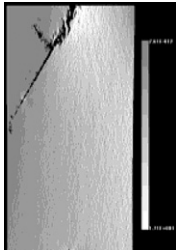
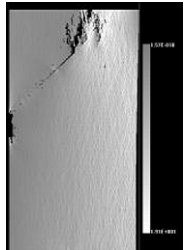
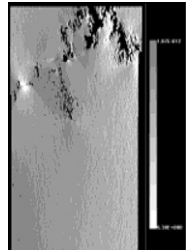
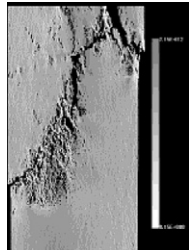
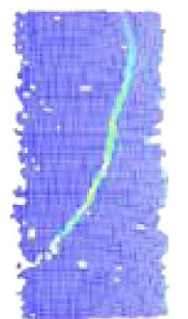
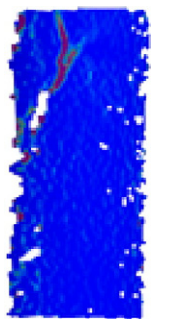
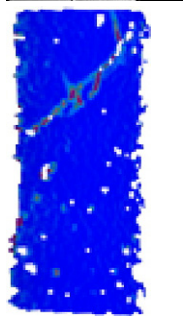
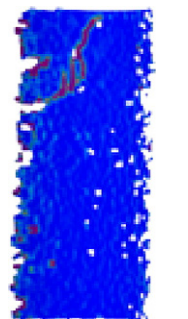
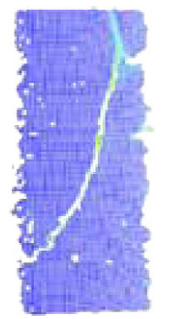

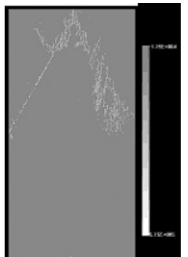
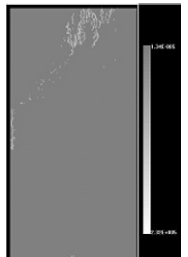
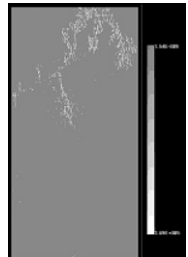
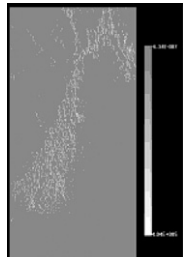
4.2. Partially-spanning joint orientation

Comparisons between the experimental and numerical results for the failure stress of specimens with various joint orientations (the angle of the joint from the plane perpendicular to the loading direction) are listed in Table 4 and plotted in Fig. 8. The experimental and numerical results show a similar trend in the compressive strength of the partially-cut specimens with various joint orientations. Although the numerical results are not completely consistent with the experimental results, the numerical failure stress falls in a reasonable range. It is noted that the influence of partially-spanning joint orientation on the compressive strength of the partially-cut specimens shows a complex relationship between joint orientation and failure stress. From the results of the UCS testing, compressive strength can be observed to decrease approximately linearly with increasing partially-spanning joint orientation value for orientations less than 45°. Conversely, for partially-spanning joint orientations greater than 45°, compressive strength can be observed to increase uniformly

with increasing orientation value. The trend of the data shown in Fig. 8 is consistent with a minimum compressive strength for specimens with a partially-spanning joint orientation of approximately 45°. The variation in strength with varying joint orientation is not consistent with the results of previous studies carried out using fully-spanning joints, the results of which support a theoretical expression that gives $(45^\circ + \phi/2)$ as the critical joint orientation for a smooth joint in terms of rock compressive strength. This indicates that the influence of a partially-spanning joint on the compressive strength of rock is different from that of a fully-spanning joint. As a result, it is unreasonable to investigate the influence of a fully-spanning joint on the mechanical behavior of jointed rocks and infer the mechanical properties of jointed rock mass, which is extensively involved in fields such as mining engineering, underground excavation and petroleum engineering.

The specimen failure patterns and corresponding strain results for the experimental and numerical results carried out on samples with varying partially-spanning joint orientations are shown in Table 5. The experimental results for failure patterns and the high local strains from ARAMIS of the samples are in good agreement with the numerical results for failure patterns and strain distributions of samples. The

Table 5
Failure patterns for experimental and numerical results for specimens with various joint orientations.

JO (°)	75	60	45	30	15
Failure pattern					
Numerical results					
ARAMIS results					
Strain distribution					

experimental and numerical results in Table 5 show that for small and large values (e.g. 15° and 75°) of partially-spanning joint orientation, the failure patterns are independent of the pre-existing joint and failure appears to have occurred entirely through virgin material. This may help to explain the observation of maximum failure stress at both low and high values of partially-spanning joint orientation, as for these situations greater energy is required to rupture the intact material than would be required to propagate the more favorably oriented partially-spanning joint in the 45° case.

Fig. 9 shows the numerically-simulated stress–strain curves and associated damage event counts of samples with varying joint orientations. It can be seen from Fig. 10 that there are few local peaks or stress drops in the complete stress–strain curves at both low and high values of partially-spanning joint orientation (e.g. 75° and 15°). Few damage events with small counts per damage event occur during the failure process of specimens and considerable damage event counts are recorded at the peak stress (see for example, the plot for joint orientation of 15° and the magnification curve prior to peak stress). In contrast, many more local peaks or stress drops can be observed in the complete stress–strain curves at medium values of partially-spanning

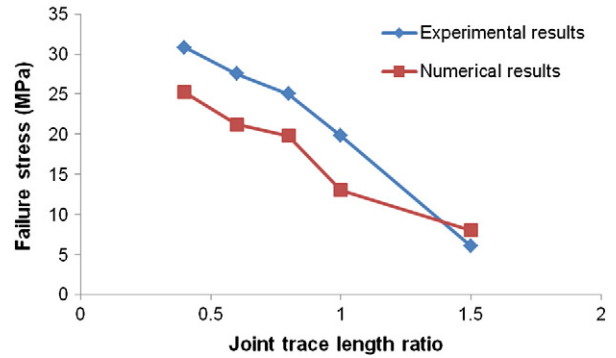
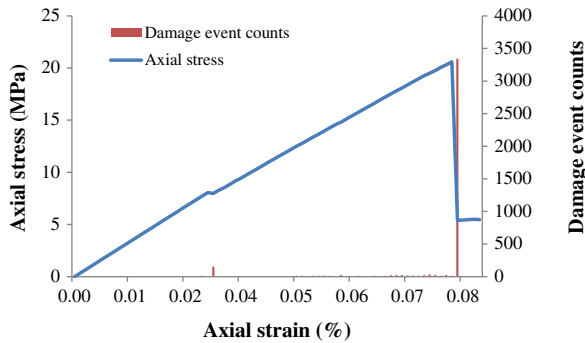
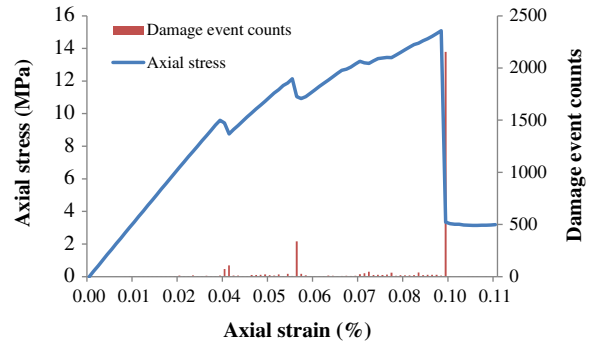


Fig. 10. Comparisons between experimental and numerical results for failure stress against joint trace length ratio.

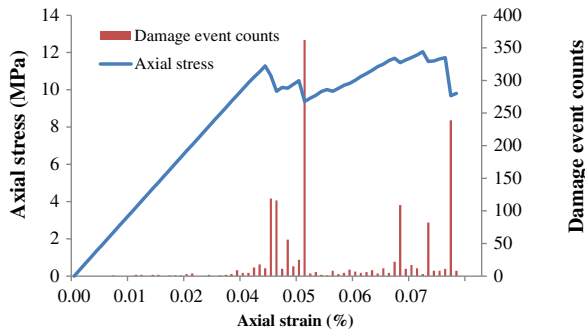
joint orientations such as 45° and 60°, in which disperse damage events with large counts per damage event occur during the rupture of the specimen. The underlying mechanism in varying damage events during the rupture of the samples with varying partially-spanning joint



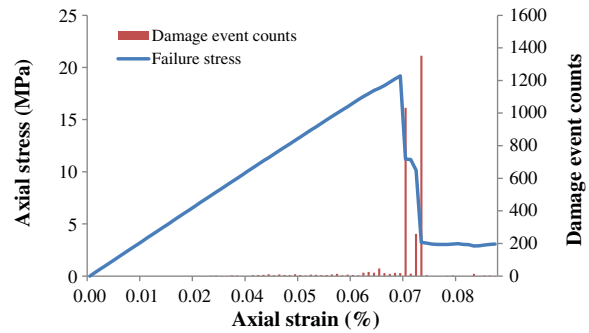
(a) 75°



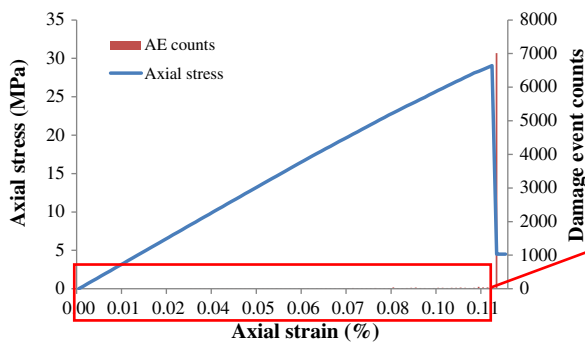
(b) 60°



(c) 45°



(d) 30°



(e) 15°

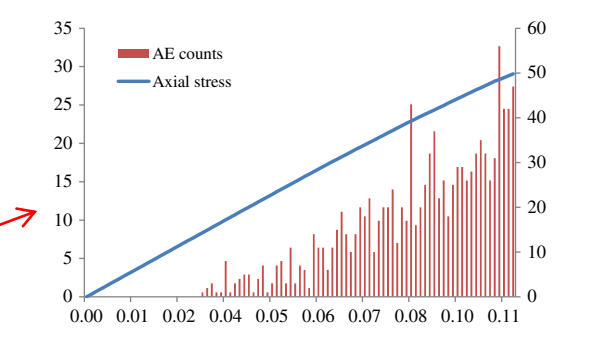


Fig. 9. Numerically simulated stress–strain and associated damage event counts vs. strain curves of specimens with different partially-spanning joint orientations (75°, 60°, 45°, 30° and 15°).

Table 6
Comparisons between experimental and numerical results for failure stress of specimens.

Joint trace length (mm)	Joint trace length ratio (D_j)	Experimental (MPa)	Numerical (MPa)	Relative error (%)
33.6	0.4	30.8	25.2	18.2
50.4	0.6	27.5	21.2	22.9
67.2	0.8	25	19.8	20.8
84	1.0	19.8	13	34.3
126	1.5	6	8	-33.3

orientations is a good analog to the fore-shock, main-shock and after-shock sequences of earthquakes around faults with varying orientations (Reasenber, 1999; Tang et al., 2003a; Wines and Lilly, 2003).

4.3. Partially-spanning joint trace length

The comparisons between experimental and numerical results for the failure stress of specimens with various joint trace lengths are listed in Table 6 and plotted in Fig. 10. As before, the experimental and numerical results show a close trend in the compressive strength of

the partially-cut specimens with various joint trace lengths. The results of the experimental and numerical tests to explore the influence of partially-spanning joint trace length on the compressive strength of specimens reveal a relationship between the partially-spanning joint trace length and the compressive strength obtained from testing. For simplicity in analysis, joint trace length is considered here as a fraction of the diameter of the specimen (ratio of trace length of the partially-spanning joint to the diameter of the specimen), and denoted as the trace length ratio, D_j . The experimental and numerical results for the failure stress of specimens with varying joint trace length ratios, D_j s and the comparisons between experimental and numerical results for failure stress of specimens are also listed in Table 6 and shown in Fig. 10, respectively. As illustrated in Fig. 10, the numerical simulations are consistent with the experimental results for specimens with varying partially-spanning joint trace length ratios, which both illustrate an approximately linear correlation between failure stress and joint trace length ratio D_j . That is to say, the higher the joint trace length ratio, the lower the compressive strength of the sample with a partially-spanning joint.

The specimen failure patterns and corresponding strain results for the experimental and numerical results tested in the study on the influence of

Table 7
Failure patterns for experimental and numerical results for specimens with various joint trace length ratios.

JTL ratio	0.4	0.6	0.8	1.0	1.5
Failure pattern					
Numerical results					
ARAMIS results					
Strain distribution					

joint trace length on failure patterns and localized deformation are shown in Table 7. The experimental and numerical results for the localized strain distribution delineate highly strained areas at the point of incipient failure. As illustrated in Table 7, the numerically simulated failure patterns are similar to the experimental results for specimens with varying partially-spanning joint trace length ratios, in which there is little difference from the experimental failure pattern for the sample with joint trace length ratio D_f of 1.0. In order to discover whether the difference between the numerical and experimental results is due to the differences between samples, additional numerical tests on the sample with D_f of 1.0 were performed, and similar failure patterns in the simulations were obtained. In addition, combined with the experimental failure patterns of samples with D_f of 0.8 and 1.5, it is inferred that the numerical failure pattern of the sample with D_f of 1.0 is reasonable and the experimental failure pattern of the sample with D_f of 1.0 is caused by sample difference. The results of Table 7 demonstrate that for specimens with longer partially-spanning joints, failure was seeded at the pre-existing flaw (joint) tip, whereas for specimens with shorter partially-spanning joints, failure was not associated with the pre-existing flaw (joint). The specimens with shorter partially-

spanning joints failed first along the partially-spanning joint, then the residual large part of the specimen underwent the applied load up to final rupture, which exhibited a high failure stress or compressive strength. In contrast, for the specimens with a longer partially-spanning joint, fracture first propagated at the tip of the longer partially-spanning joint along the direction of the maximum principal stress, and the mechanical properties of the specimens deteriorated greatly and could not bear a high stress, and thus the samples exhibited a low failure stress or compressive strength. The greater amount of material rupture required for failure of the shorter partially-spanning joints may explain the observation of maximum compressive strength for the lowest values of joint trace length.

Fig. 11 shows the numerically-simulated stress–strain curves and associated damage event counts of samples with varying joint trace length ratios. It is seen from Fig. 11 that the partially-spanning joint trace length ratio has an obvious influence on the stress–strain curves and the overall mechanical behavior of the samples with a partially-spanning joint. There are few local peaks or stress drops in the complete stress–strain curves at both low values of partially-spanning joint trace length ratios. Few damage events with small counts per damage event

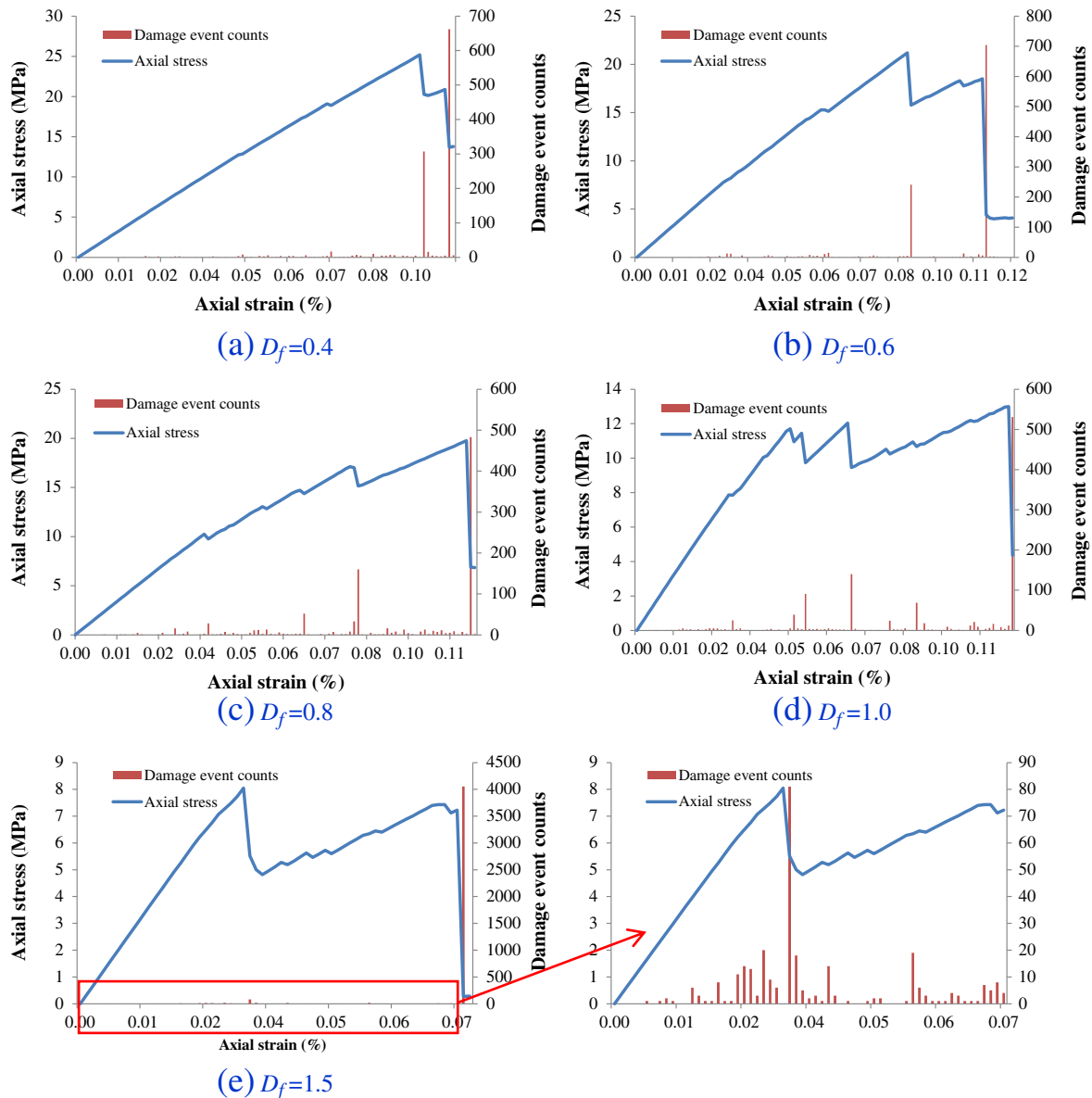


Fig. 11. Numerically-simulated stress–strain and associated damage event counts vs. strain curves of specimens with different partially-spanning joint trace length ratios D_f s.

occur during the failure process of the specimen and considerable damage event counts are recorded at the peak stress. In contrast, many more local peaks or stress drops can be observed in the complete stress–strain curves at higher values of partially-spanning joint trace length ratio, in which dispersed damage events with large counts per damage event occur during the rupture of the specimen, as seen in the plot for the joint trace length ratio of 1.5 and the amplification curve prior to peak stress.

5. Conclusions

In this paper, uniaxial compressive testing of plane stress numerical specimens with an embedded, partially-spanning joint was used to investigate the individual influence of three parameters relating to the geometry of partially-spanning joints: joint location, joint orientation and joint trace length (ratio). The numerical simulations not only agree well with the experimental results, but also duplicate the complete rupture process of samples with the stress evolution and tempo-spatial distribution of damage events.

With respect to joint location, the numerical simulations demonstrate an approximately linear relationship between the location of the terminus of the partially-spanning joint with respect to the end of the sample (joint location) and the compressive strength of the partially-cut sample, whereby failure stress increases with increasing joint location value. This suggests that a greater length of material to be ruptured to cause failure will require more energy input for failure. In relation to joint orientation, the test results show that minimum compressive strength occurs for a joint angle of 45°, and that compressive strength increases with both increasing joint angle and decreasing joint angle from this critical value of 45°. The nature of the curve relating the compressive strength obtained from numerical simulations and experiments to the orientation of the partially-spanning joints tested is such that the slope defined by variation in compressive strength with increasing joint angle from 45° is different from the slope defined by variation in compressive strength with decreasing joint angle from 45°. These results differ from results obtained for similar testing using fully-spanning joints, suggesting that relationships obtained from work on fully-spanning joints cannot be directly applied to cases concerning partially-spanning joints. In relation to joint trace length (ratio), numerical simulations reveal that the compressive strength of partially-cut specimens can be correlated with joint trace length (ratio) using a linear relationship. In addition, the joint trace length (ratio) has an obvious influence on the stress–strain curves of samples with a partially-spanning joint.

In general, the results of a numerical study conducted on specimens with partially-spanning joints in different geometries were compared with the experimental results. Numerical simulations duplicate the stress field in the vicinity of cracks, and capture the associated damage event sequence, the process of propagation, and the coalescence of cracks in samples with a partially-spanning joint. The results show that the failure stress and failure patterns of samples strongly depend on the mechanical and geometric properties of partially-spanning joints in samples, and the failure of jointed samples in axial compression is the final manifestation of earlier tensile crack growth induced under overall compression. Numerical simulations demonstrate some simple relationships between compressive strength of a rock-like material with partially-spanning joints and the geometry of those partially-spanning joints. These relationships differ in nature from those found for fully-spanning joints. This indicates that it is of great importance to have a clear understanding of the geometry of the joints in jointed rock prior to the design of engineering rock mass structures. The work reported in this paper is an initial effort on the influence of joint geometry on the strength of jointed rocks containing partially-spanning joints. The numerical simulations provide a fundamental understanding of damage and failure behavior in a jointed rock mass and the numerical tool employed in this paper can be used to

efficiently study the complex damage and failure behavior of jointed rock mass with complicated multiple joints.

Acknowledgments

The support provided by the National Natural Science Foundation of China (Grant no. 41172265) and the National Basic Research Program of China (2013CB227900) is gratefully acknowledged.

References

- Bobet, A., Einstein, H., 1998a. Fracture coalescence in rock-type materials under uniaxial and biaxial compression. *Int. J. Rock Mech. Min. Sci.* 35, 863–888.
- Bobet, A., Einstein, H., 1998b. Numerical modeling of fracture coalescence in a model rock material. *Int. J. Fract.* 92, 221–252.
- Brady, B.H.G., Brown, E.T., 2004. *Rock Mechanics for Underground Mining*. Kluwer Academic Publishers, London.
- Brekke, T.L., Selmer-Olsen, R., 1965. Stability problems in underground constructions caused by montmorillonite-carrying joints and faults. *Eng. Geol.* 1, 3–19.
- Chakraborty, A.K., Jethwa, J.L., Paithankar, A.G., 1994. Effects of joint orientation and rock mass quality on tunnel blasting. *Eng. Geol.* 37, 247–262.
- Chen, X., Liao, Z., Peng, X., 2012. Deformability characteristics of jointed rock masses under uniaxial compression. *International Journal of Mining Science and Technology* 22, 213–221.
- Deb, D., Das, K.C., 2009. Extended finite element method (XFEM) for analysis of cohesive rock joint. *J. Sci. Ind. Res.* 68, 575–583.
- Fairhurst, C., Hudson, J., 1999. Draft ISRM suggested method for the complete stress–strain curve for intact rock in uniaxial compression. *Int. J. Rock Mech. Min. Sci.* 36, 279–289.
- Giacomini, A., Buzzi, O., Ferrero, A.M., Migliazza, M., Giani, G.P., 2008. Numerical study of flow anisotropy within a single natural rock joint. *Int. J. Rock Mech. Min. Sci.* 45, 47–58.
- Griffith, A.A., 1921. The phenomena of rupture and flow in solids. *Philos. Trans. R. Soc. Lond. Ser. A* 221, 163–198.
- Huang, J., Chen, G., Zhao, Y., Wang, R., 1990. An experimental study of the strain field development prior to failure of a marble plate under compression. *Tectonophysics* 175, 269–284.
- Hudson, J.A., Brown, E., Fairhurst, C., 1971. Optimizing the control of rock failure in servo-controlled laboratory tests. *Rock Mech. Rock. Eng.* 3, 217–224.
- Hudson, J.A., Crouch, S.L., Fairhurst, C., 1972. Soft, stiff and servo-controlled testing machines: a review with reference to rock failure. *Eng. Geol.* 6, 155–189.
- Ingraffea, A.R., Heuze, F.E., 1980. Finite element models for rock fracture mechanics. *Int. J. Numer. Anal. Methods Geomech.* 4, 25–43.
- Jeager, J.C., Cook, N.G.W., Zimmerman, R., 2007. *Fundamentals of Rock Mechanics*, 4th ed. Wiley-Blackwell, Singapore.
- Kemeny, J.M., 1991. A model for non-linear rock deformation under compression due to sub-critical crack growth. *Int. J. Rock Mech. Min. Sci. Geomech. Abstr.* 28, 459–467.
- Kemeny, J.M., 2003. The time-dependent reduction of sliding cohesion due to rock bridges along discontinuities: a fracture mechanics approach. *Rock Mech. Rock. Eng.* 36, 27–38.
- Kemeny, J.M., 2005. Time-dependent drift degradation due to the progressive failure of rock bridges along discontinuities. *Int. J. Rock Mech. Min. Sci.* 42, 35–46.
- Lajtai, E.Z., 1975. Failure along planes of weakness. *Can. Geotech. J.* 12, 118–125.
- Lemaître, J., Desmorat, R., 2005. *Engineering Damage Mechanics*. Springer-Verlag, Berlin.
- Lin, C.T., Amadei, B., Jung, J., Dwyer, J., 1996. Extensions of discontinuous deformation analysis for jointed rock masses. *Int. J. Rock Mech. Min. Sci. Geomech. Abstr.* 33, 671–694.
- Ma, G.W., An, X.M., Zhang, H.H., Li, L.X., 2009. Modeling complex crack problems using the numerical manifold method. *Int. J. Fract.* 156, 21–35.
- Okubo, S., Nishimatsu, Y., 1985. Uniaxial compression testing using a linear combination of stress and strain as the control variable. *Int. J. Rock Mech. Min. Sci. Geomech. Abstr.* 22, 323–330.
- Petit, J.-P., Barquins, M., 1988. Can natural faults propagate under mode II conditions? *Tectonics* 7, 1243–1256.
- Prudencio, M., Van Sint Jan, M., 2007. Strength and failure modes of rock mass models with non-persistent joints. *Int. J. Rock Mech. Min. Sci.* 44, 890–902.
- Ramamurthy, T., Arora, V.K., 1994. Strength predictions for jointed rocks in confined and unconfined states. *Int. J. Rock Mech. Min. Sci. Geomech. Abstr.* 31, 9–22.
- Reasenber, P.A., 1999. Foreshock occurrence before large earthquakes. *J. Geophys. Res.* 104, 4755–4768.
- Shen, B., Stephansson, O., Einstein, H.H., Ghahreman, B., 1995. Coalescence of fractures under shear stresses in experiments. *J. Geophys. Res. Solid Earth* 100, 5975–5990.
- Shi, G.H., 1988. *Discontinuous Deformation Analysis: A New Numerical Model for the Statics and Dynamics of Block Systems*. (PhD thesis) University of California, Berkeley.
- Steif, P.S., 1984. Crack extension under compressive loading. *Eng. Fract. Mech.* 20, 463–473.
- Tang, C.A., Kou, S.Q., 1998. Crack propagation and coalescence in brittle materials under compression. *Eng. Fract. Mech.* 61, 311–324.
- Tang, C.A., Huang, M.L., Zhao, X.D., 2003a. Weak zone related seismic cycles in progressive failure leading to collapse in brittle crust. *Pure Appl. Geophys.* 160, 2319–2328.
- Tang, C.A., Wang, S.H., Fu, Y.F., 2003b. Numerical Tests on Rock Failure Process. Science Press, Beijing (in Chinese).
- Tang, C.A., Wong, R.H.C., Chau, K.T., Lin, P., 2005. Modeling of compression-induced splitting failure in heterogeneous brittle porous solids. *Eng. Fract. Mech.* 72, 597–615.

- Tang, C.A., Zhang, Y.B., Liang, Z.Z., Xu, T., Tham, L.G., Lindqvist, P.A., Kou, S.Q., Liu, H.Y., 2006. Fracture spacing in layered materials and pattern transition from parallel to polygonal fractures. *Phys. Rev. E* 73, 0561201–0561209.
- Tang, C.A., Liang, Z.Z., Zhang, Y.B., Chang, X., Xu, T., Wang, D.G., Zhang, J.X., Liu, J.S., Zhu, W.C., Elsworth, D., 2008. Fracture spacing in layered materials: a new explanation based on two-dimensional failure process modeling. *Am. J. Sci.* 308, 49–72.
- Vásárhelyi, B., Bobet, A., 2000. Modeling of crack initiation, propagation and coalescence in uniaxial compression. *Rock Mech. Rock. Eng.* 33, 119–139.
- Wasantha, P.L.P., Ranjith, P.G., Viete, D.R., 2012a. Constitutive models describing the influence of the geometry of partially-spanning joints on jointed rock mass strength: regression and fuzzy logic analysis of experimental data. *Expert Syst. Appl.* 39, 7663–7672.
- Wasantha, P.L.P., Ranjith, P.G., Viete, D.R., Luo, L., 2012b. Influence of the geometry of partially-spanning joints on the uniaxial compressive strength of rock. *Int. J. Rock Mech. Min. Sci.* 50, 140–146.
- Weibull, W., 1951. A statistical distribution function of wide applicability. *J. Appl. Mech.* 18, 293–297.
- Wines, D.R., Lilly, P.A., 2003. Estimates of rock joint shear strength in part of the Fimiston open pit operation in Western Australia. *Int. J. Rock Mech. Min. Sci.* 40, 929–937.
- Wong, R.H.C., Chau, K.T., 1998. Crack coalescence in a rock-like material containing two cracks. *Int. J. Rock Mech. Min. Sci.* 35, 147–164.
- Wong, R.H.C., Chau, K.T., Tang, C.A., Lin, P., 2001. Analysis of crack coalescence in rock-like materials containing three flaws — part I: experimental approach. *Int. J. Rock Mech. Min. Sci.* 38, 909–924.
- Wu, Z., Wong, L.N.Y., 2012. Frictional crack initiation and propagation analysis using the numerical manifold method. *Comput. Geotech.* 39, 38–53.
- Wu, Z., Wong, L.N.Y., 2013. Modeling cracking behavior of rock mass containing inclusions using the enriched numerical manifold method. *Eng. Geol.* 162, 1–13.
- Xu, T., Tang, C.A., Zhang, Z., Zhang, Y.B., 2003. Theoretical, experimental and numerical studies on deformation and failure of brittle rock in uniaxial compression. *J. Northeast. Univ.* 24, 87–90 (in Chinese).
- Xu, T., Tang, C.A., Wang, S.Y., Zhao, X.D., 2004. Influence of crack continuity on propagation of en echelon cracks in heterogeneous materials. *J. Northeast. Univ.* 25, 167–170.
- Xu, T., Tang, C.A., Zhao, J., Li, L.C., Heap, M.J., 2012. Modelling the time-dependent rheological behaviour of heterogeneous brittle rocks. *Geophys. J. Int.* 189, 1781–1796.
- Zhang, X., Sanderson, D.J., 2001. Evaluation of instability in fractured rock masses using numerical analysis methods: effects of fracture geometry and loading direction. *J. Geophys. Res. Solid Earth* 106, 26671–26687.
- Zhang, X.P., Wong, L., 2012. Cracking processes in rock-like material containing a single flaw under uniaxial compression: a numerical study based on parallel bonded-particle model approach. *Rock Mech. Rock. Eng.* 45, 711–737.
- Zhang, X.P., Wong, L., 2013. Crack initiation, propagation and coalescence in rock-like material containing two flaws: a numerical study based on bonded-particle model approach. *Rock Mech. Rock. Eng.* 46, 1001–1021.
- Zhang, H.H., Li, L.X., An, X.M., Ma, G.W., 2010. Numerical analysis of 2-D crack propagation problems using the numerical manifold method. *Eng. Anal. Bound. Elem.* 34, 41–50.